

Amides inventory towards the G+0.693-0.027 molecular cloud

S. Zeng,^{1*} V. M. Rivilla,² I. Jiménez-Serra,² L. Colzi,² J. Martín-Pintado,²
B. Tercero,^{3,4} P. de Vicente,⁴ S. Martín,^{5,6} and M. A. Requena-Torres⁷

¹Star and Planet Formation Laboratory, Cluster for Pioneering Research, RIKEN, 2-1 Hirosawa, Wako, Saitama, 351-0198, Japan

²Centro de Astrobiología (CSIC-INTA), Ctra. de Ajalvir Km. 4, 28850, Torrejón de Ardoz, Madrid, Spain

³Observatorio Astronómico Nacional (OAN-IGN), Calle Alfonso XII, 3, 28014 Madrid, Spain

⁴Observatorio de Yebes (OY-IGN), Cerro de la Palera s/n, Yebes, 19141, Guadalajara, Spain

⁵European Southern Observatory, Alonso de Córdova 3107, Vitacura 763-0355, Santiago, Chile

⁶Joint ALMA Observatory, Alonso de Córdova 3107, Vitacura 763-0355, Santiago, Chile

⁷Department of Physics, Astronomy and Geosciences, Towson University, Towson, MD 21252, USA

Accepted XXX. Received YYY; in original form ZZZ

ABSTRACT

Interstellar amides have attracted significant attentions as they are potential precursors for a wide variety of organics essential to life. However, our current understanding of their formation in space is heavily based on observations in star-forming regions and hence the chemical networks lack the constraints on their early origin. In this work, unbiased sensitive spectral surveys with IRAM 30m and Yebes 40m telescopes are used to systematically study a number of amides towards a quiescent Galactic Centre molecular cloud, G+0.693-0.027. We report the first detection of acetamide ($\text{CH}_3\text{C}(\text{O})\text{NH}_2$) and trans-N-methylformamide (CH_3NHCHO) towards this cloud. In addition, with the wider frequency coverage of the survey, we revisited the detection of formamide (NH_2CHO) and urea (carbamide; $\text{NH}_2\text{C}(\text{O})\text{NH}_2$), which had been reported previously towards G+0.693-0.027. Our results are compared with those present in the literature including recent laboratory experiments and chemical models. We find constant abundance ratios independently of the evolutionary stages, suggesting that amides related chemistry is triggered in early evolutionary stages of molecular cloud and remain unaffected by the warm-up phase during the star formation process. Although a correlation between more complex amides and NH_2CHO have been suggested, alternative formation routes involving other precursors such as acetaldehyde (CH_3CHO), methyl isocyanate (CH_3NCO) and methylamine (CH_3NH_2) may also contribute to the production of amides. Observations of amides together with these species towards a larger sample of sources can help to constrain the amide chemistry in the interstellar medium.

Key words: ISM: molecules – ISM: clouds – Galaxy: centre – galaxies: ISM – astrochemistry – line: identification

1 INTRODUCTION

Amides are chemical species that contain a carbonyl group linked to a nitrogen atom ($\text{R}_1-\text{C}(=\text{O})-\text{N}-\text{R}''$), which can also be referred to as peptide bonds during the formation of proteins, where a large number of amino acids bind with each other through peptide chains. Amides are thus among the essential components in the fundamental building blocks of life that make up the structural components of living cells and regulate biochemical processes (Ruiz-Mirazo et al. 2014). The presence of amino acids on the prebiotic Earth is widely accepted, either coming from endogenous chemical processes (e.g. Patel et al. 2015) or forming in the interstellar medium (ISM), and with their subsequent delivery to Earth (e.g. Altwegg et al. 2016). As such, understanding the formation of amides in the ISM can be relevant for studying the chemical origin of life.

Formamide (NH_2CHO) was the first amide detected in the ISM (towards Sgr B2; Rubin et al. 1971) and has then been robustly detected in several star-forming regions (see e.g. very recent observations by Colzi et al. 2021; Ligterink et al. 2020, 2022, and see

review by López-Sepulcre et al. 2019 for a detailed list of astronomical observations). Ever since the detection of formamide, amides with increasing complexity such as acetamide ($\text{CH}_3\text{C}(\text{O})\text{NH}_2$; Hollis et al. 2006; Halfen et al. 2011; Belloche et al. 2017; Ligterink et al. 2020, 2022; Colzi et al. 2021), and N-methylformamide (CH_3NHCHO ; Belloche et al. 2017; Ligterink et al. 2020, 2022; Colzi et al. 2021) have been detected in the ISM, although mostly exclusively towards high-mass star-forming regions. The detection of another amide, urea (aka carbamide, $\text{NH}_2\text{C}(\text{O})\text{NH}_2$), has also been confirmed towards the Galactic Centre (GC) source Sgr B2(N1) (Belloche et al. 2019) and the molecular cloud G+0.693-0.027 (Jiménez-Serra et al. 2020). However, searches of more complex amides such as cyanofornamide (NH_2COCN) and glycolamide ($\text{HOCH}_2\text{C}(\text{O})\text{NH}_2$) in the ISM have been attempted without success (Colzi et al. 2021; Ligterink et al. 2022; Sanz-Novo et al. 2022).

To get insight into how complex the interstellar chemistry is and what prebiotic molecules can be synthesised in space, it is essential to understand the chemical processes that result in the formation of simpler amides detected in the ISM. For the aforementioned amides, both gas-phase and grain formation routes have been discussed to explain their observed abundance in the regions where they reside

* E-mail: shaoshan.zeng@riken.jp

(e.g. Jones et al. 2011; Skouteris et al. 2017; Quénard et al. 2018; Belloche et al. 2019; Douglas et al. 2022; Garrod et al. 2022).

For example, tight column density correlation is found between NH_2CHO and $\text{CH}_3\text{C(O)NH}_2$, which might indicate these two species are formed through related chemical processes or have the same responses to similar physical conditions (Colzi et al. 2021; Ligterink et al. 2022). However, detection of several amides from the same regions are still relatively sparse and they are biased towards the physical conditions of star-forming regions. The chemical networks that include amides may therefore lack of further constraints to elucidate the chemical link between these species and the interplay with the physical conditions especially at earliest stage of star formation.

In this work, the most complete inventory of amide species is investigated in detail towards the quiescent molecular cloud G+0.693-0.027 (hereafter G+0.693). G+0.693 is located within the Sgr B2 star-forming complex in the center of our Galaxy. Despite the fact it does not show signs of on-going star-formation activity (Zeng et al. 2020), it represents one of the most chemically rich sources in our Galaxy. With plentiful of nitrogen-bearing species detected towards G+0.693, the family of nitrile ($-\text{CN}$) and amines ($-\text{NH}_2$) as well as several complex organic molecules (COMs) that are of pre-biotic interest have also been reported in previous studies (Zeng et al. 2018; Rivilla et al. 2019, 2020, 2021a,b, 2022b; Bizzocchi et al. 2020; Rodríguez-Almeida et al. 2021a; Zeng et al. 2021). Following up the detection of NH_2CHO (Zeng et al. 2018) and $\text{NH}_2\text{C(O)NH}_2$ (Jiménez-Serra et al. 2020), additional transitions of these species along with the first detection of $\text{CH}_3\text{C(O)NH}_2$ and CH_3NHCHO towards G+0.693 is presented in Section 2 and 3. The possible formation routes for each amide are discussed in 4 whilst the conclusions are given in Section 5.

2 OBSERVATIONS

The high-sensitivity spectral surveys towards G+0.693 molecular cloud were carried out with IRAM 30 m¹ and Yebes 40 m² telescopes. The IRAM 30 m observations were performed during three sessions in 2019: 10th–16th of April, 13th–19th of August, and 11th–15th of December whilst the observations with the Yebes 40 m telescope were carried out through project 20A008 between 3rd–9th and 15th–22nd of February 2020. The observations were centred at $\alpha(\text{J2000}) = 17^{\text{h}}47^{\text{m}}22^{\text{s}}$, $\delta(\text{J2000}) = -28^{\circ}21'27''$. The position switching mode was used in all observations with the reference position located at $\Delta\alpha$, $\Delta\delta = -885'', 290''$ with respect to the source position. The IRAM 30 m observations covered the frequency ranges of 71.8–116.7 GHz, 124.8–175.5 GHz, 199.8–222.3 GHz, and 223.3–238.3 GHz. The half-power beam width (HPBW) of the telescope spanned between $\sim 34'' - 11''$. The spectral coverage of Yebes 40 m observations ranged from 31.3 GHz to 50.6 GHz. The HPBW of the telescope was in a range of $\sim 54'' - 36''$. The data from both surveys were smoothed to a velocity resolution of $\sim 1.0 - 2.6 \text{ km s}^{-1}$ and the intensity was measured in the unit of antenna temperature, T_{A}^* , as the molecular emission towards G+0.693 is extended over the beam (Requena-Torres et al. 2006, 2008; Zeng et al. 2020). Depending on the frequency, the noise of the spectra for the Yebes 40 m data is 1.0 mK, whilst in some intervals can increase up to 4.0–5.0 mK;

¹ IRAM is supported by INSU/CNRS (France), MPG (Germany), and IGN (Spain)

² The 40 m radiotelescope at Yebes Observatory is operated by the Spanish Geographic Institute (IGN, Ministerio de Transportes, Movilidad y Agenda Urbana.) <http://rt40m.oan.es/rt40men.php>

whereas 1.3 to 2.8 mK (71–90 GHz), 1.5 to 5.8 mK (90–115 GHz), $\sim 10 \text{ mK}$ (115–116 GHz), 3.1 to 6.8 mK (124–175 GHz), and 4.5 to 10.6 mK (199–238 GHz), for the IRAM 30 m data. More detailed information of these observations is provided in Zeng et al. (2020); Rodríguez-Almeida et al. (2021b).

3 ANALYSIS AND RESULTS

The line identification and the analysis were carried out using the SLIM (Spectral Line Identification and Modelling) tool implemented within the MADCUBA package³ (version 10/03/2022, Martín et al. 2019). SLIM uses the spectroscopic entries from the Cologne Database for Molecular Spectroscopy⁴ (CDMS, Endres et al. 2016), the Jet Propulsion Laboratory⁵ (JPL, Pickett et al. 1998), and our own database with added entries for species that are not included in the previous catalogue by using available spectroscopic literature. SLIM generates synthetic spectra under the assumption of Local Thermodynamic Equilibrium (LTE) conditions and taking into account the line opacity. For the molecules presented in this work, the spectroscopic information is given in Table A1 in Appendix A. In order to properly evaluate the potential line contamination, the emission from over 125 molecules identified towards G+0.693 have been considered (Requena-Torres et al. 2006, 2008; Rivilla et al. 2018, 2019, 2020, 2021a,b, 2022a,b,c; Bizzocchi et al. 2020; Jiménez-Serra et al. 2020, 2022; Rodríguez-Almeida et al. 2021a,b; Zeng et al. 2018, 2021). The AUTOFIT tool of SLIM was used to provide the best non-linear least-squares LTE fit to the data using the Levenberg-Marquardt algorithm, which provides the value and uncertainty of the physical parameters for each molecular species (see detailed description in Martín et al. 2019). The free parameters of the model are: molecular column density (N_{tot}), excitation temperature (T_{ex}), central radial velocity (v_{LSR}), and full width half maximum (FWHM). Figure 1–5 present, in the order of increasing rest frequency, the unblended or slightly blended transitions of the molecules studied in this work. The emission of the other transitions as predicted by LTE are consistent with the fitted spectra, but they are severely blended with lines arising from other molecular species. The fitting parameters together with the derived column density and the molecular abundance with respect to molecular hydrogen, assuming $N_{\text{H}_2} = 1.35 \times 10^{23} \text{ cm}^{-2}$ (Martín et al. 2008), of each molecule are summarised in Table 1. The transitions used for the LTE fits are listed in Table A2.

3.1 New detections

Acetamide ($\text{CH}_3\text{C(O)NH}_2$)

Acetamide ($\text{CH}_3\text{C(O)NH}_2$) is an asymmetric top molecule that has an internal rotation of the methyl group, making its spectrum complicated. The dipole moments of $\text{CH}_3\text{C(O)NH}_2$ are $\mu_a = 1.14 \text{ D}$ and $\mu_b = 3.5 \text{ D}$ (Hollis et al. 2006). In this work, both a- and b-type transitions at the ground torsional state were detected but b-type were predominant. For clarity, we adopt the same labelling convention $J''_{K''_a, K''_c} - J'_{K'_a, K'_c}$ for the A- and E-states of acetamide as Hollis et al. (2006). Out of 79 unblended or slightly blended transitions, the energy range covered in the 34 E-state transitions (Figure 1) and the 45 A-state transitions (Figure 2) is $E_u = 9.7 - 35.7 \text{ K}$

³ Madrid Data Cube Analysis on ImageJ is a software developed at the Center of Astrobiology (CAB) in Madrid; <http://cab.inta-csic.es/madcuba/>

⁴ <https://cdms.astro.uni-koeln.de/classic/>

⁵ <https://spec.jpl.nasa.gov/ftp/pub/catalog/catdir.html>

Table 1. Physical parameters obtained from the best LTE fit in MADCUBA and derived molecular abundance with respect to H₂.

Molecule	T_{ex} (K)	v_{LSR} (km s ⁻¹)	FWHM (km s ⁻¹)	N_{tot} ($\times 10^{13}$ cm ⁻²)	X^a ($\times 10^{-10}$)
NH ₂ ¹³ CHO	5.0±0.3	69.1±0.6	21±1	0.62±0.04	0.46±0.03
NH ₂ CHO ^c	-	-	-	25±1	18±1
CH ₃ C(O)NH ₂ A	7.4±0.2	68.7±0.3	19.5±0.6	3.4±0.1	2.50±0.07
CH ₃ C(O)NH ₂ E	7.8±0.1	68.7±0.2	21.6±0.4	8.1±0.1	6.0±0.1
CH ₃ C(O)NH ₂ (A+E)	-	-	-	11.5±0.2	8.5±0.1
trans-CH ₃ NHCHO	7.1±0.4	68.2±0.5	19±1	4.3±0.4	3.2±0.3
NH ₂ C(O)NH ₂	8.0±0.7	69 ^d	20 ^b	0.71±0.05	0.52±0.05

^a $N_{\text{H}_2}=1.35\times 10^{23}$ cm⁻² (Martín et al. 2008).

^b Value of FWHM fixed in the MADCUBA fit.

^c Column density and abundance derived from the ¹³C-isotopologue by multiplying ¹²C/¹³C=40 (Colzi et al. in prep).

^d Value of v_{LSR} fixed in the MADCUBA fit.

and $E_u=3.0\text{--}48.2$ K respectively. The best LTE fit finds good agreement in excitation conditions between A- and E-state transitions. For E-state, $T_{\text{ex}}=7.8\pm 0.1$ K, $v_{\text{LSR}}=68.7\pm 0.2$ km s⁻¹ and FWHM=21.6±0.4 km s⁻¹ whilst for A-state, $T_{\text{ex}}=7.4\pm 0.2$ K, $v_{\text{LSR}}=68.7\pm 0.3$ km s⁻¹, and FWHM=19.5±0.6 km s⁻¹. The derived column density for E- and A-state is $N_{\text{tot}}=(8.1\pm 0.1)\times 10^{13}$ cm⁻² and $N_{\text{tot}}=(3.4\pm 0.1)\times 10^{13}$ cm⁻² respectively, yielding an E/A ratio of 2.4±0.1 towards G+0.693 which is in agreement with the one, E/A = 1.9, derived from the colder more extended molecular gas towards Sgr B2(N) at an excitation temperature of 5.8 K (Remijan et al. 2022). In contrast, an E/A ratio of 0.75 is obtained from the hot core region towards Sgr B2(N) at an excitation temperature of 170 K (Belloche et al. 2013). While the E/A ratio of CH₃C(O)NH₂ seems to vary with the excitation temperature, more detections of both E- and A-type CH₃C(O)NH₂ are needed to reach a conclusion. The total column density by summing up both states is $N_{\text{tot}}=(1.15\pm 0.02)\times 10^{14}$ cm⁻², which translates to a molecular abundance of $(8.5\pm 0.1)\times 10^{-10}$.

Trans-N-methylformamide (CH₃NHCHO)

N-methylformamide is an isomer of CH₃C(O)NH₂ and it exists in two forms, *trans* and *cis*, with the former being more stable (by 466 cm⁻¹ or 666 K; Kawashima et al. 2010). In this work, both E- and A-state transitions from the ground torsional state of trans-N-CH₃NHCHO are detected. Unlike CH₃C(O)NH₂, the same physical parameters as well as column densities were derived from both E- and A-state trans-CH₃NHCHO. In total, 26 unblended or slightly blended transitions, 7 E-state transitions and 19 A-state transitions, were detected towards G+0.693 (Figure 3). The upper state energy ranges in $E_u=2.2\text{--}28.2$ K. The best LTE fit gives $T_{\text{ex}}=7.1\pm 0.4$ K, $v_{\text{LSR}}=68.2\pm 0.5$ km s⁻¹, FWHM=19±1 km s⁻¹, and $N_{\text{tot}}=(4.3\pm 0.4)\times 10^{13}$ cm⁻². This translates into a molecular abundance of $(3.2\pm 0.3)\times 10^{-10}$.

3.2 Revisit

Formamide (NH₂CHO)

The detection of formamide (NH₂CHO) was reported towards G+0.693 by Zeng et al. (2018). However, with the new dataset used in this study, it is confirmed that the NH₂CHO emission suffers from optical depth effect. Therefore, we have derived the column density of NH₂CHO using the optically thin ¹³C isotopologue. Six unblended or slightly blended transitions ($E_u = 3.1\text{--}15.2$ K; Figure 4) are identified. The best-fit parameters obtained by AUTOFIT

are $T_{\text{ex}}=5.0\pm 0.3$ K, $v_{\text{LSR}}=69.1\pm 0.6$ km s⁻¹, FWHM=21±1 km s⁻¹, and $N_{\text{tot}}=(6.2\pm 0.4)\times 10^{12}$ cm⁻². Assuming ¹²C/¹³C=40 measured in G+0.693 by Colzi et al. (in prep.), the inferred column density for NH₂CHO is $(2.5\pm 0.1)\times 10^{14}$ cm⁻² and the corresponding molecular abundance for NH₂CHO is of $(1.8\pm 0.1)\times 10^{-9}$.

3.3 Urea (NH₂C(O)NH₂)

Urea (NH₂C(O)NH₂), also known as carbamide, has a dipole moment of $\mu=\mu_b=3.83$ D (Brown et al. 1975). A total of 15, among which 8 transitions have already been reported by Jiménez-Serra et al. (2020), unblended or slightly blended transitions were detected towards G+0.693. The upper state energy ranges $E_u=2.9\text{--}25.7$ K. With v_{LSR} and FWHM fixed to 69 km s⁻¹ and 20 km s⁻¹, the best LTE fit gives $T_{\text{ex}}=8.0\pm 0.7$ K and $N_{\text{tot}}=(7.1\pm 0.5)\times 10^{12}$ cm⁻². This translates into a molecular abundance of $(5.2\pm 0.5)\times 10^{-11}$, which is consistent to that reported by Jiménez-Serra et al. (2020).

4 DISCUSSION

The amides detection presented in Section 3 has not only expanded the number of species identified in G+0.693, but also offers an opportunity to study the chemical processes leading to amides formation in a region unaffected by star formation. Although G+0.693 is located in the same molecular cloud complex as the high-mass star-forming region Sgr B2(N), the kinematic and chemical study of Zeng et al. (2020) showed that the overall distribution of molecular gas towards G+0.693 depicted a different morphology and structure to that of Sgr B2(N). Furthermore, observational signatures of a cloud-cloud collision have been detected at small scales (0.2 pc), which agrees well with previous observations at larger scales in the Sgr B2 region as reported in literature (e.g. Hasegawa et al. 1994; Tsuboi et al. 2015). As a consequence, shocks associated with the cloud-cloud collision are expected to sputter efficiently the icy grain mantles in G+0.693, subsequently ejecting materials formed on grains into the gas phase including complex organic molecules. Note that G+0.693 is located at a about ~2.4 pc away in projected distance from the Sgr B2(N) high-mass star-forming region (assuming a distance of 8.178 kpc for the Galactic Centre; GRAVITY Collaboration et al. 2019), distant enough to make it unlikely that the star-formation activity of the Sgr B2(N) star cluster affects the chemistry of the G+0.693 cloud. Recent study of deuteration fractionation towards this source proposed that G+0.693 is on the verge of star formation (Colzi et al. 2022) i.e. under prestellar conditions, which is likely due to the event

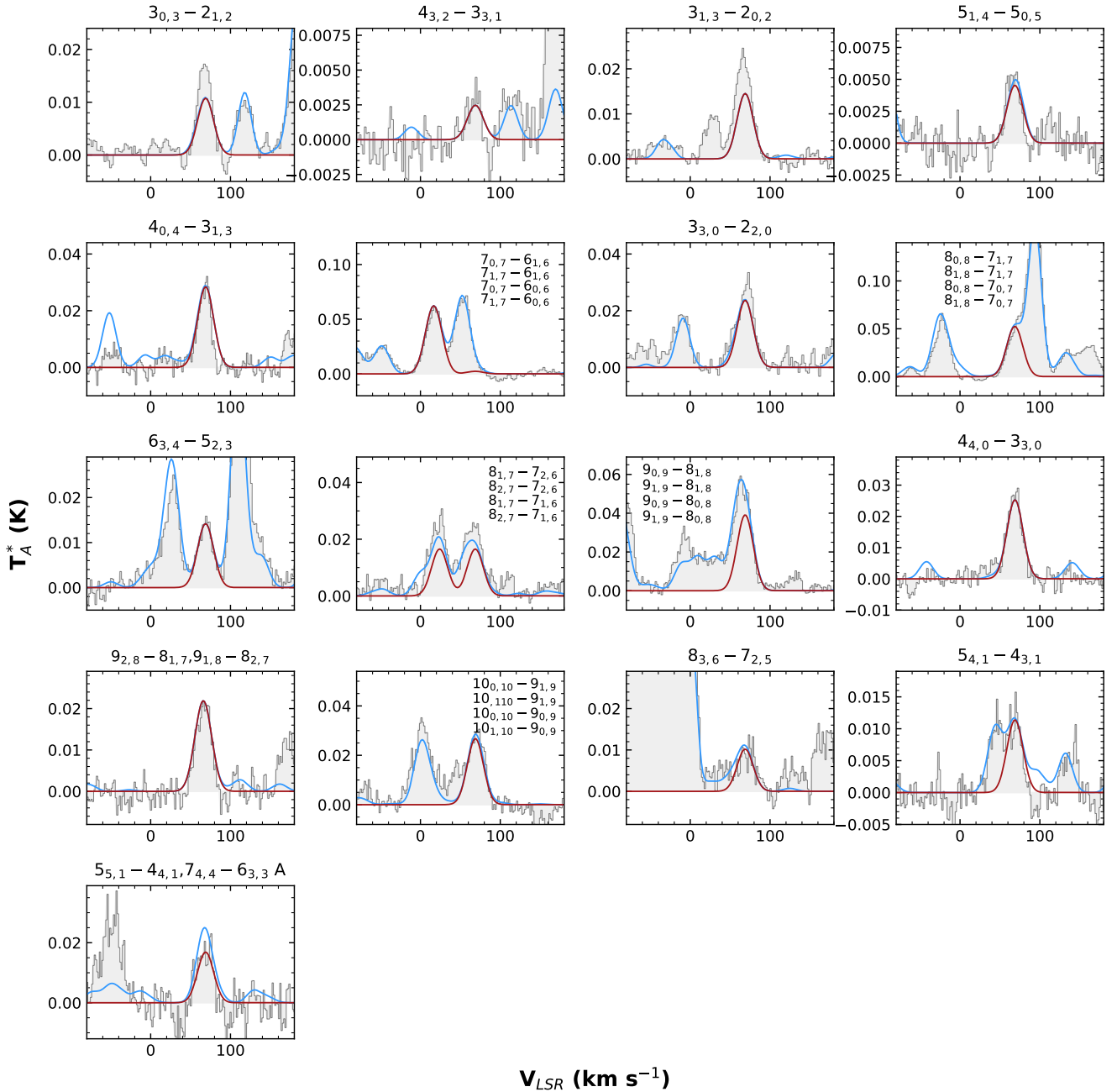


Figure 1. Detected E-state transitions of $\text{CH}_3\text{C}(\text{O})\text{NH}_2$ towards G+0.693. The observed spectrum is plotted in grey, with the best LTE fit obtained with MADCUBA overplotted in red and the synthetic spectrum considering contribution from all the species identified in the source is indicated by the blue line. The quantum number of each transition is given on the top of each panel.

of a cloud-cloud collision. All this makes the conditions driving the chemistry of G+0.693 differ substantially from typical star-forming sources such as the nearby Sgr B2(N) hot core since the lack of protostellar heating implies that the thermal evaporation of ices is not yet playing a relevant role. Because amides have mostly been studied in star-forming regions, a comparison between these regions and G+0.693 could be useful to provide better constraints on the formation routes of amide species. In the following sections, comparison of molecular abundance of NH_2CHO with respect to H_2 is presented in Fig. 6 whilst molecular ratios with respect to NH_2CHO derived towards G+0.603 are compared to those obtained from other in-

terstellar sources (see Fig. 7). The comparison are made primarily towards star-forming sources in which the inventory of amides has been investigated in detail. The possible formation mechanisms of amide species, as summarised in Figure 8, are discussed along with available laboratory experiments, chemical models, and theoretical studies. To clarify, the term fast, medium, and slow models mentioned in the following section is referred to the model with warm-up timescales of 5×10^4 yr, 2×10^5 yr, and 1×10^6 yr, respectively as they are defined in Belloche et al. (2017, 2019) and Garrod et al. (2022).

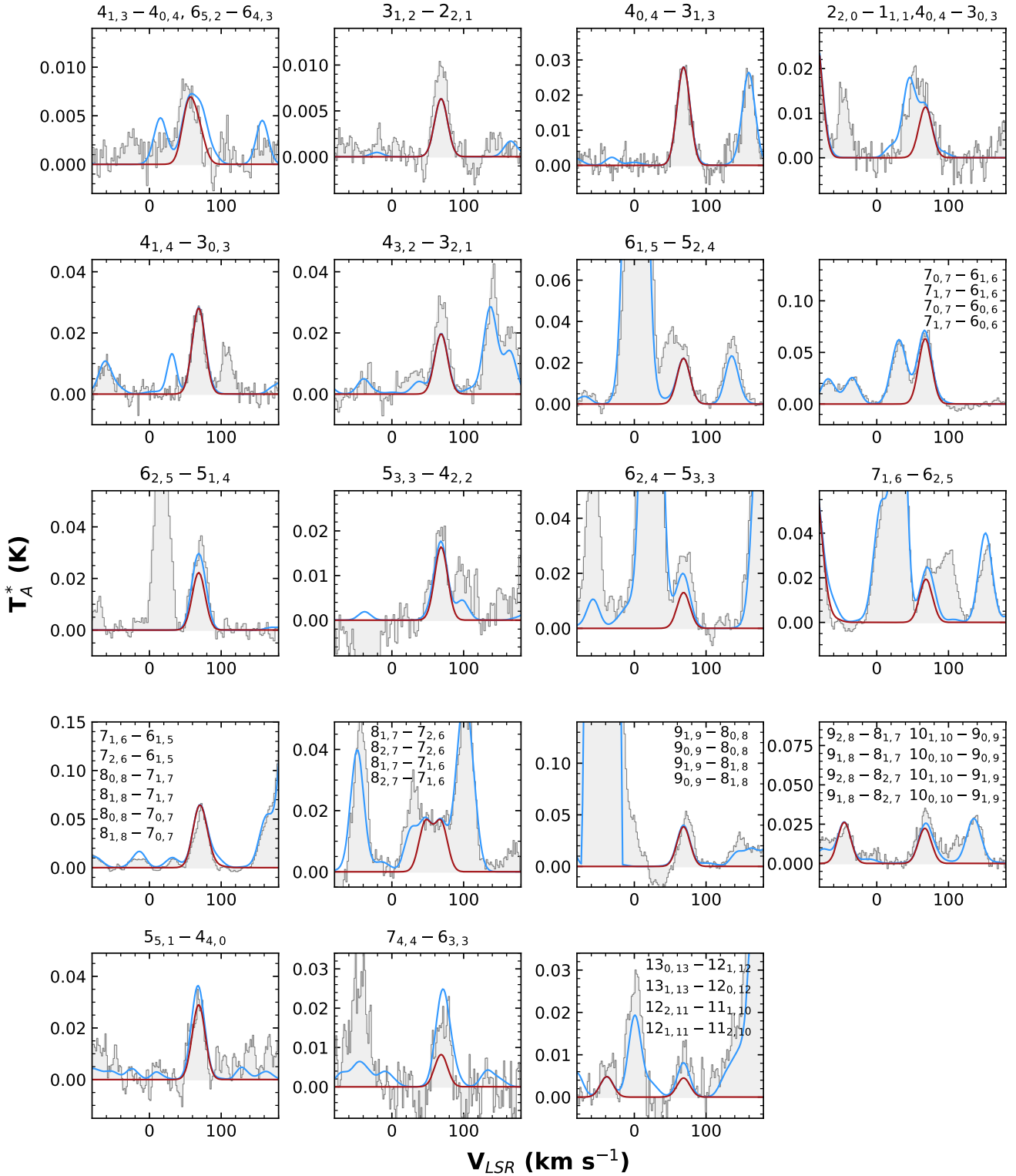


Figure 2. Detected A-state transitions of $\text{CH}_3\text{C}(\text{O})\text{NH}_2$ towards G+0.693. The observed spectrum is plotted in grey, with the best LTE fit obtained with MADCUBA overplotted in red and the synthetic spectrum considering contribution from all the species identified in the source is indicated by the blue line. The quantum number of each transition is given on the top of each panel.

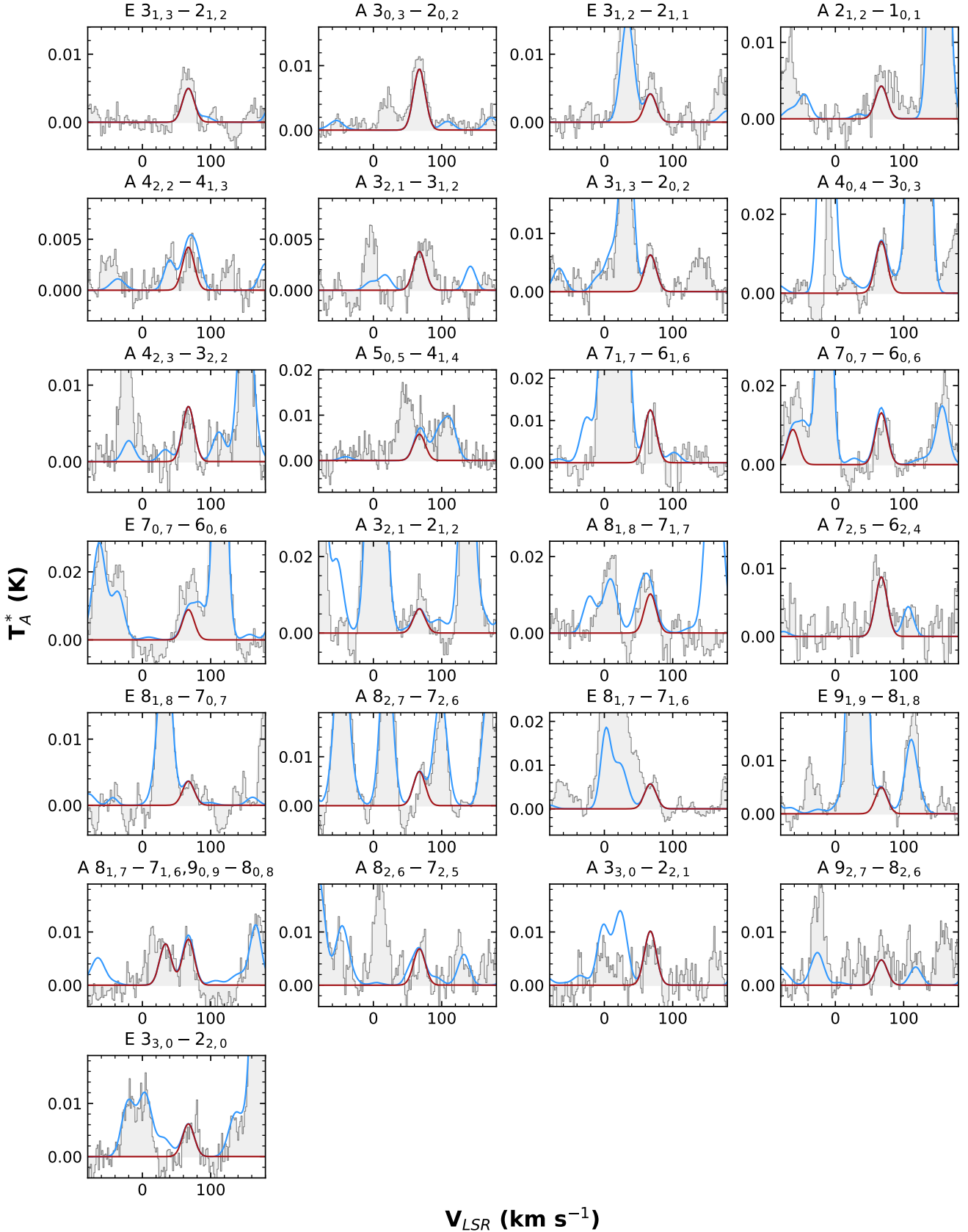


Figure 3. Detected transitions of CH₃NHCHO towards G+0.693. The observed spectrum is plotted in grey, with the best LTE fit obtained with MADCUBA overlotted in red and the synthetic spectrum considering contribution from all the species identified in the source is indicated by the blue line. The quantum number of each transition is given on the top of each panel.

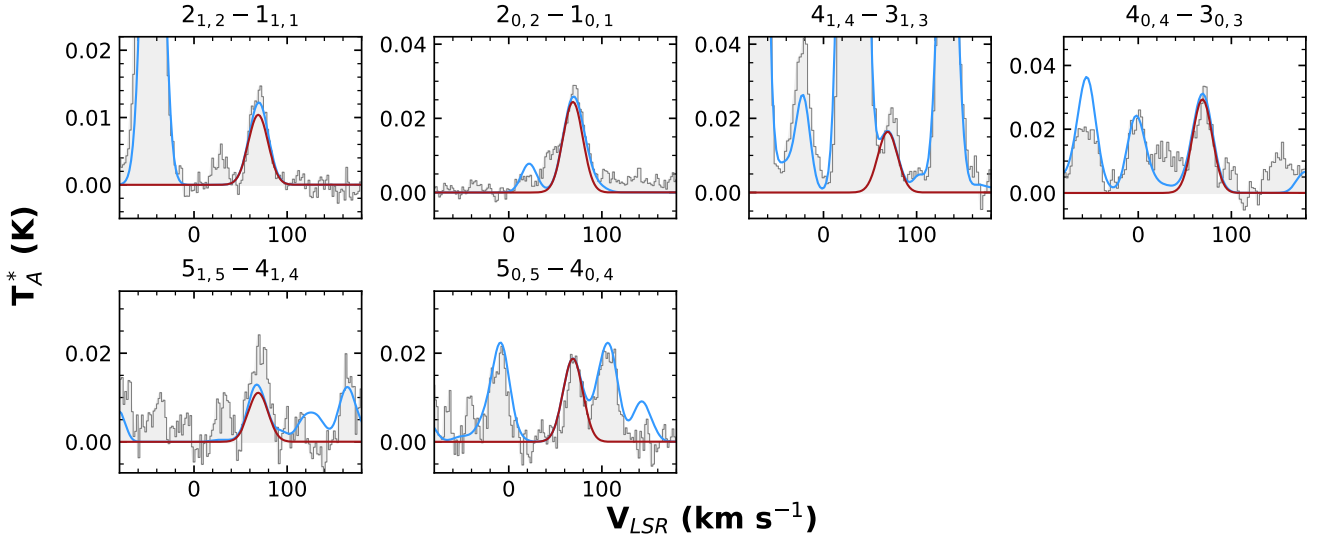


Figure 4. Detected transitions of $\text{NH}_2^{13}\text{CHO}$ towards G+0.693. The observed spectrum is plotted in grey, with the best LTE fit obtained with MADCUBA overlotted in red and the synthetic spectrum considering contribution from all the species identified in the source is indicated by the blue line. The quantum number and the upper state energy of each transition is given on the top of each panel.

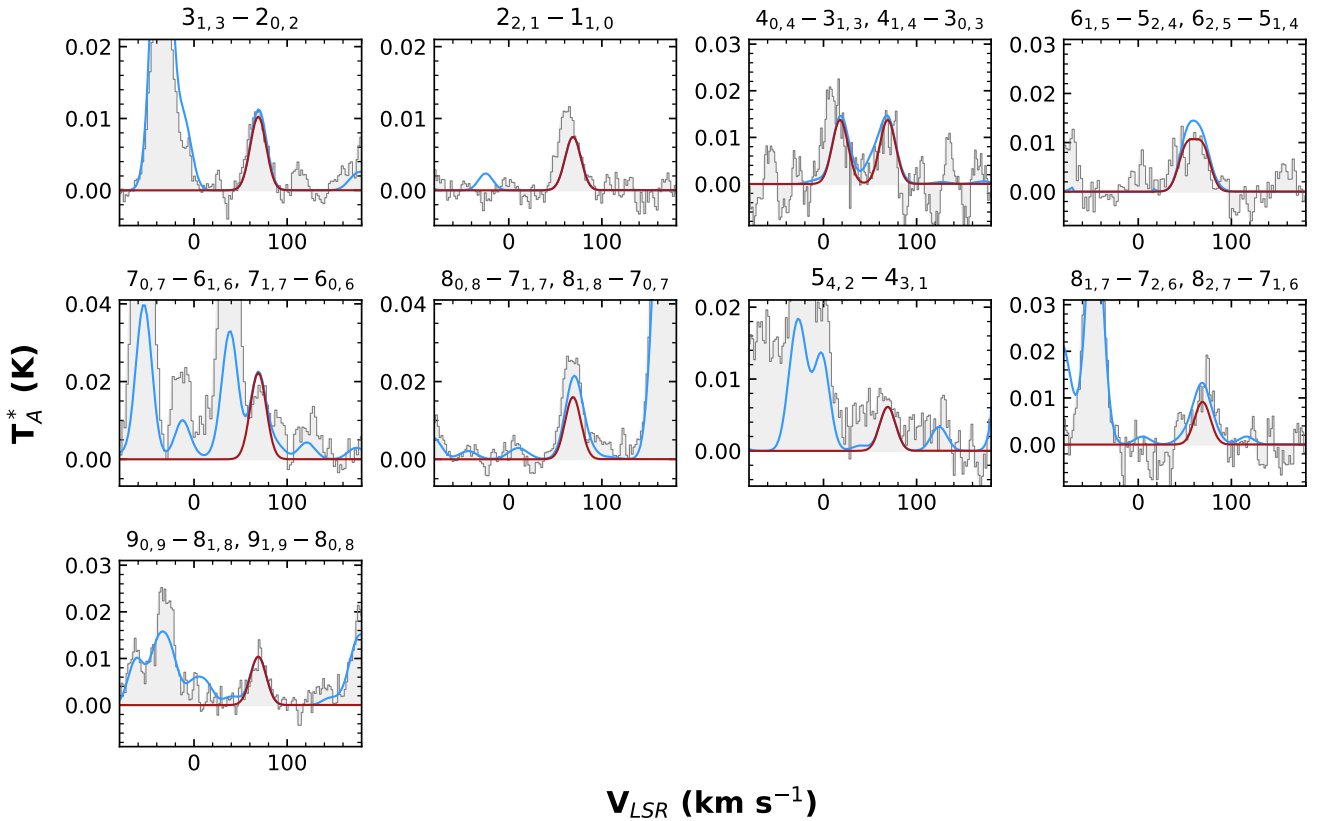


Figure 5. Detected transitions of $\text{NH}_2\text{C}(\text{O})\text{NH}_2$ towards G+0.693. The observed spectrum is plotted in grey, with the best LTE fit obtained with MADCUBA overlotted in red and the synthetic spectrum considering contribution from all the species identified in the source is indicated by the blue line. The quantum number of each transition is given on the top of each panel.

4.1 Formamide

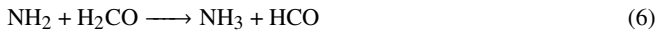
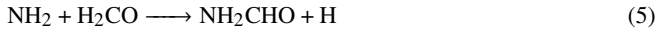
NH_2CHO is the smallest molecule to contain a peptide bond and hence often considered as a potential precursor of a wide variety of organic compounds essential to life. As reviewed by López-Sepulcre et al. (2019), both theoretical and experimental studies have investigated the formation mechanism of NH_2CHO . However, it is still strongly debated whether its formation is governed by gas-phase reactions or grain-surface chemistry. On grain surfaces, the popular route of successive HNC0 hydrogenation (reaction 1 and 2) was ruled out by the experimental work of Noble et al. (2015) but disputed with the dual-cyclic mechanism of H-atom abstraction and addition reactions by Haupa et al. (2019).



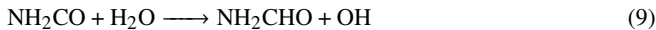
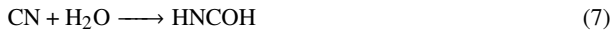
Another frequently studied formation route on the grain surface is the radical-radical recombination of NH_2 and HCO (reaction 3). It should proceed without any activation barrier; however, the two radicals are required to be in close proximity and a competing reaction (reaction 4) could lead back to the formation of NH_3 and CO (Rimola et al. 2018; Chuang et al. 2022).



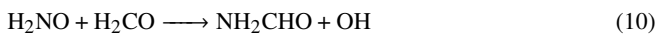
Similar to reaction (3), a competing H-abstraction reaction is expected for radical-molecule reaction proposed by Fedoseev et al. (2016):



Other surface reactions involving different precursors have also been proposed for the NH_2CHO formation. Through quantum chemical computations, Rimola et al. (2018) suggested a series of reactions forming NH_2CHO started by CN:



Laboratory experiments performed by Dulieu et al. (2019) demonstrated that NH_2CHO formation is possible from barrierless hydrogenation of NO followed by the radical-radical addition reaction with H_2CO (reaction 10). However, under the conditions of typical molecular cloud i.e. at 10 K, NO and H_2CO are not mobile on the grain surface and hence their proximity represents the limiting factor of this formation route.



In the gas phase, reaction (5) has been studied theoretically as a gas-phase pathway (Barone et al. 2015; Skouteris et al. 2017). However, its feasibility was challenged by Song & Kästner (2016) and more recently by Douglas et al. (2022). The latter reported a significant energy barrier of the reaction and concluded that it is not an important source of NH_2CHO at low temperatures in interstellar environments. Note that at high temperatures, Quénard et al. (2018) also showed

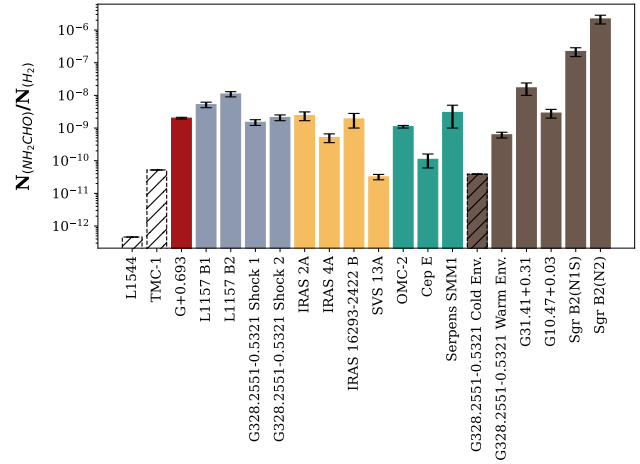


Figure 6. Bar plot of NH_2CHO abundance with respect to H_2 towards various interstellar regions. Sources with different physical conditions are represented in different colours: red = molecular cloud; grey = shocked regions; yellow = low-mass star-forming sources; green = intermediate star-forming sources; brown = high-mass star-forming sources. Upper limits of NH_2CHO are denoted in striped bar. Data are taken from: G+0.693 (this work), L1157 (Mendoza et al. 2014), IRAS 2A and IRAS 4A (Taquet et al. 2015), IRAS 16293 B (Martín-Doménech et al. 2017), L1544, TMC-1, SVS 13A, OMC-2, and Cep E (López-Sepulcre et al. 2015), Serpens SMM1 (Ligterink et al. 2022), G31.41+0.31 (Colzi et al. 2021), G10.47+0.03 (Gorai et al. 2020), G328.2551-0.5321 (Bouscasse et al. 2022), Sgr B2 (N1S) and (N2)) (Belloche et al. 2017, 2019). For Sgr B2 (N1S) and (N2), H_2 column density of $1.31 \times 10^{25} \text{ cm}^{-2}$ and $1.6 \times 10^{24} \text{ cm}^{-2}$ respectively, are adapted from Bonfand et al. (2017).

that the formation of NH_2CHO is dominated by grain surface reactions, thus its gas phase formation is not sufficient to reproduce the observations.

In Figure 6, the molecular abundance of NH_2CHO with respect to H_2 derived towards G+0.693 is compared to a diverse set of interstellar regions, including pre-stellar sources (L1544 and TMC-1), shocked regions (G+0.693, L1157, and G328.2551-0.5321 shock 1,2), low-mass (IRAS 2A, IRAS 4A, IRAS 16293-2422 B, SVS 13A), intermediate-mass (OMC-2, Cep E, Serpens SMM1), and high-mass star-forming sources (G31.41+0.31, G10.47+0.03, G328.2551-0.5321, Sgr B2N). To simplify, only sources with determined H_2 column densities were selected. In line with the conclusions of Colzi et al. (2021) and Ligterink et al. (2022), the lack of detection towards pre-stellar sources and the comparable abundance of NH_2CHO between shocked regions and star-forming regions reveal that NH_2CHO is commonly formed in the ice mantles of grains and released back to gas-phase via non-thermal/thermal processes. In particular, the NH_2CHO abundance in G+0.693 is comparable, within a factor of 6, to the ones obtained in the shocked region L1157, G328.2551-0.5321 shock 1 and 2, suggesting that molecules detected towards G+0.693 have been freshly desorbed from the dust mantles as a result of grain-sputtering. The large abundance of NH_2CHO found in high-mass star-forming regions suggests that its formation could be boosted by the warm up of the grains due to star formation. However, this seems to be inconsistent with the constant abundance ratios, indicating that the formation might partly be occurring during the pre-stellar phase as supported by recent chemical modelling (Garrod et al. 2022). In addition, relatively lower abundance of NH_2CHO in low-mass and intermediate-mass star-forming regions hints at a difference in the heating timescale.

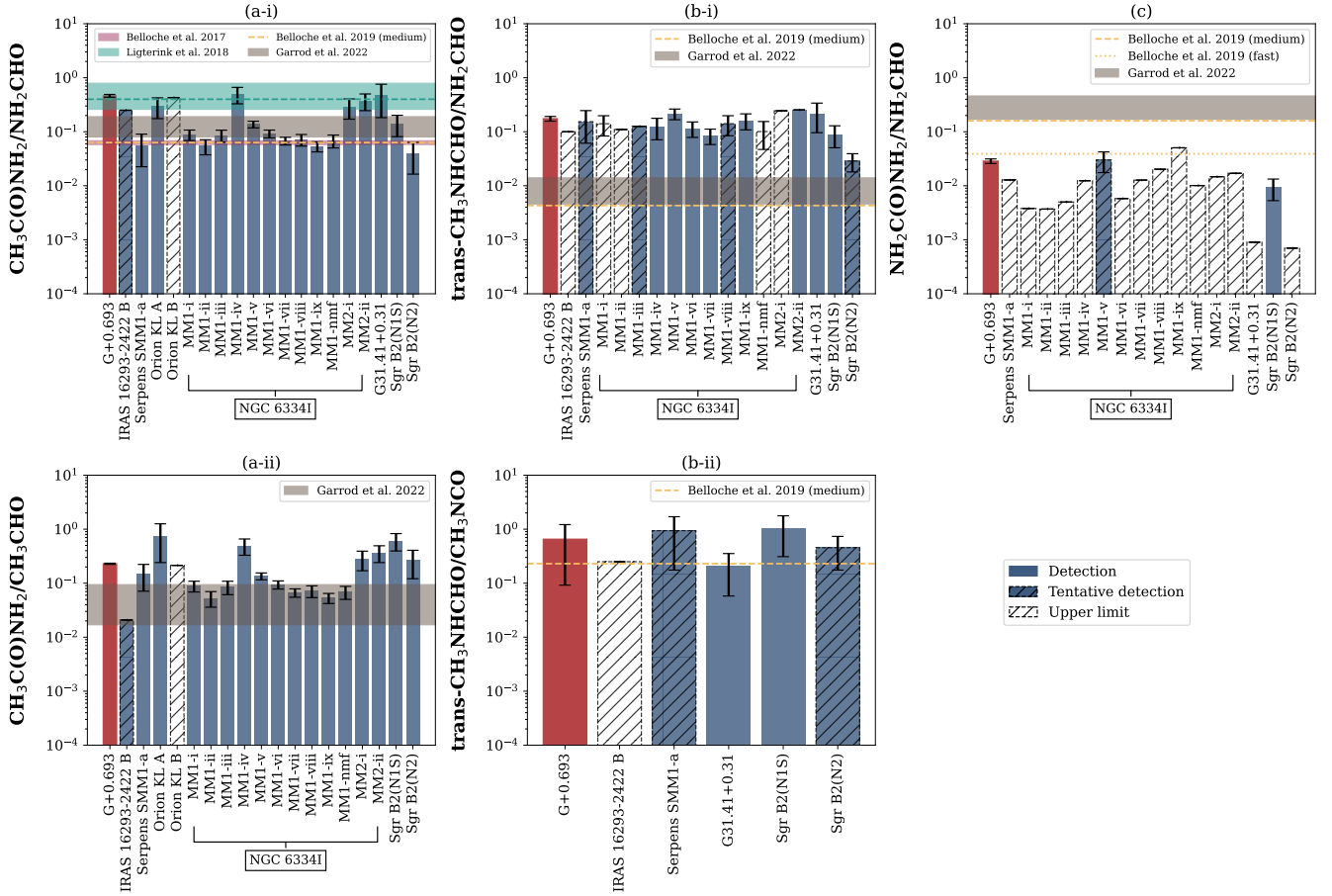
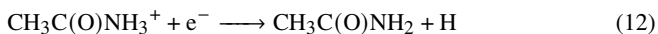
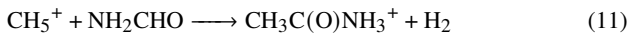


Figure 7. (a-i): Ratio of $\text{CH}_3\text{C}(\text{O})\text{NH}_2/\text{NH}_2\text{CHO}$. (a-ii): Ratio of $\text{CH}_3\text{C}(\text{O})\text{NH}_2/\text{CH}_3\text{CHO}$. (b-i): Ratio of $\text{trans-N-CH}_3\text{NHCHO}/\text{NH}_2\text{CHO}$. (b-ii): Ratio of $\text{trans-N-CH}_3\text{NHCHO}/\text{CH}_3\text{NCO}$. (e): Ratio of $\text{NH}_2\text{C}(\text{O})\text{NH}_2/\text{NH}_2\text{CHO}$. The green, brown, and pink shaded area denote the results from laboratory experiment by Ligterink et al. (2018) and chemical models by Belloche et al. (2017) and Garrod et al. (2022), respectively. The yellow dashed line and dotted line indicates the result from the best matching model, medium or fast, of Belloche et al. (2019) respectively. Observational data are taken from: G+0.693 (this work), IRAS 16293 B (Coutens et al. 2016; Lykke et al. 2017; Ligterink et al. 2018), Serpens SMM1 (Ligterink et al. 2022), Orion KL (Cernicharo et al. 2016), NGC 6334I (Ligterink et al. 2020), G31.41+0.31 (Colzi et al. 2021), Sgr B2(N1S) and (N2) (Belloche et al. 2017, 2019).

4.2 Acetamide

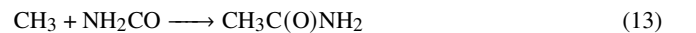
The formation of $\text{CH}_3\text{C}(\text{O})\text{NH}_2$ has been suggested to be dependent on the production of NH_2CHO (e.g. Hollis et al. 2006). From an observational point of view, the column density of $\text{CH}_3\text{C}(\text{O})\text{NH}_2$ is found to tightly correlate with that of NH_2CHO (e.g. Colzi et al. 2021; Ligterink et al. 2022). The origin of this correlation could indicate a direct chemical link or the same response to the environmental conditions such as temperature for HNC and NH_2CHO (Quénard et al. 2018).

Chemically, the ion-molecule reaction (reaction 11 and 12) between protonated methane (CH_5^+) and neutral NH_2CHO followed by electron recombination is considered to be the most efficient process among various gas phase reactions proposed for $\text{CH}_3\text{C}(\text{O})\text{NH}_2$ formation (Halfen et al. 2011; Redondo et al. 2014).



On the surface of dust grains, $\text{CH}_3\text{C}(\text{O})\text{NH}_2$ is considered to be predominately formed by the addition of CH_3 to NH_2CO radical (reaction 13) and the latter links $\text{CH}_3\text{C}(\text{O})\text{NH}_2$ and NH_2CHO through

several possible reactions.



In recent chemical models, this radical is considered to be formed by H-abstraction from NH_2CHO , addition of H to HNC, and/or radical addition of $\text{NH}_2 + \text{CO}$ (Belloche et al. 2017, 2019; Garrod et al. 2022). In the case of H-abstraction from NH_2CHO , Belloche et al. (2017) found a $\text{CH}_3\text{C}(\text{O})\text{NH}_2/\text{NH}_2\text{CHO}$ ratio of 0.06–0.07 (denoted as pink shaded area in Figure 7-(a-i)). In contrast, Garrod et al. (2022) determined the ratio of 0.08–0.19 (denoted as brown shaded area in Figure 7-(a-i)) by considering both the H addition to HNC and reaction of NH_2 with CO in the bulk ice for the NH_2CO radical production. The derived $\text{CH}_3\text{C}(\text{O})\text{NH}_2/\text{NH}_2\text{CHO}$ ratio in G+0.693 is 0.43 ± 0.03 which is at least a factor of two higher than the model predicted ratios. We note that these models are for hot cores where thermal desorption dominates the ejection of molecules to gas phase from grains. But since the formation of $\text{CH}_3\text{C}(\text{O})\text{NH}_2$ is likely dominated by grain surface chemistry, some insights might be provided by making the comparison between the observational results in G+0.693 and these chemical models. In fact, several high-mass star-forming regions such as Orion KL, NGC 6334I (MM1-iv, MM2-i, and MM2-ii), and G31.41+0.31 also show $\text{CH}_3\text{C}(\text{O})\text{NH}_2/\text{NH}_2\text{CHO}$ ratios close

to that found in G+0.693 (see Figure 7-(a-i)). Additionally, this ratio determined towards G+0.693 is consistent with the results from laboratory experiment in which $\text{CH}_4\text{-HNCO}$ ice mixtures at 20 K were irradiated with far-UV photons to produce the radicals required for the formation of the amides (green shaded area in 7-(a-i); Ligterink et al. 2018). The resulting $\text{CH}_3\text{C(O)NH}_2/\text{NH}_2\text{CHO}$ ratio is $0.4^{+0.39}_{-0.14}$ and the NH_2CO radical is proposed to form via the radical addition of $\text{NH}_2 + \text{CO}$. The good match suggests that the formation pathway of both NH_2CHO and $\text{CH}_3\text{C(O)NH}_2$ on dust grains in G+0.693 are similar to the chemical processes mimicked on laboratory ices i.e. NH_2CHO formed via reaction (3) and $\text{CH}_3\text{C(O)NH}_2$ formed via reaction (13), of which the NH_2CO radical is the product of $\text{NH}_2 + \text{CO}$. Therefore, both species might not be directly connected in chemistry but likely share a common chemical origin, similar to the scenario explained by Garrod et al. (2022) for HNCO and NH_2CO . Since G+0.693 is shielded from direct UV irradiation, the key intermediate radicals are likely produced by cosmic ray-induced UV field instead. It is noteworthy that the reaction of $\text{NH}_2 + \text{HCO}$ is found to be negligible compared with both the abstraction of hydrogen from NH_2CHO and the addition of H to HNCO in chemical models by setting a typical value of activation energy barrier to 2500 K (Belloche et al. 2019). Therefore, constraining the activation barriers and rate coefficient of the processes that lead to NH_2CO , the key intermediate, is one essential step to better elucidate the formation of $\text{CH}_3\text{C(O)NH}_2$.

In the literature, there are other alternative mechanisms proposed for the formation of $\text{CH}_3\text{C(O)NH}_2$. For instance, one involves addition of NH_2 radical to CH_3CO (reaction (14)), which may also be important to form $\text{CH}_3\text{C(O)NH}_2$ on dust grain surfaces (Belloche et al. 2017; Ligterink et al. 2018; Belloche et al. 2019; Garrod et al. 2022).



The CH_3CO could be formed by H-abstraction of acetaldehyde (CH_3CHO) which is similar to the H abstraction of NH_2CHO . Towards G+0.693, the abundance of CH_3CHO is derived to be 3.7×10^{-9} (Sanz-Novo et al. 2022) and it is approximately as abundant as NH_2CHO . Therefore the formation pathway of $\text{NH}_2 + \text{CH}_3\text{CO}$ seems to be feasible in G+0.693. In the study of Ligterink et al. (2018), CH_3CHO was not detected in the laboratory experiments which raised the speculation of this formation route to proceed on ices, but it could not be completely ruled out. In recent chemical models (see brown shaded area in Figure 7-(a-ii) Belloche et al. 2019; Garrod et al. 2022), this formation route is included as modest contribution to form $\text{CH}_3\text{C(O)NH}_2$ and it is found to become important at around $T=50$ K in a slow warm-up model. However, the ratio of $\text{CH}_3\text{C(O)NH}_2/\text{CH}_3\text{CHO}$ does not vary significantly (within a factor of 5) between G+0.693, whose dust temperature typically lie below 20 K (Rodríguez-Fernández et al. 2004; Guzmán et al. 2015), and star-forming sources (Figure 7-(a-ii)). The comparison here points towards the idea that reaction (14) may have contribution to the formation of $\text{CH}_3\text{C(O)NH}_2$ but not the dominant mechanism on the grain surface.

4.3 Trans-N-methylformamide

As for the trans-N- $\text{CH}_3\text{NHCHO}/\text{NH}_2\text{CHO}$ ratio, a scatter of less than a factor of 3, except Sgr B2(N2), is found across various sources. The consistent results between G+0.693 and star-forming sources indicates that the tentative correlation between trans-N- CH_3NHCHO and NH_2CHO hold also at an early stage of star formation and the

formation route of trans-N- CH_3NHCHO could be similar among all these sources.

On grain surfaces, trans-N- CH_3NHCHO is considered to be linked to NH_2CHO by the reaction of $\text{HNCHO} + \text{CH}_3$ (Belloche et al. 2017; Ligterink et al. 2018; Garrod et al. 2022):



The HNCHO radical is an isomer of NH_2CO . Although it is unclear how these two species differ in term of reactivity, HNCHO should be more stable than NH_2CO since the molecular orbital of the unpaired electron held by the nitrogen atom could be stabilised by hyperconjugation by the C–O π bond (J. Garcia de la Concepcion, private communication). HNCHO can be formed via the radical addition of $\text{NH} + \text{CHO}$, but H-addition yielding NH_2CHO is expected to occur subsequently. Whilst H-abstraction from NH_2CHO seems to strongly favour the production of NH_2CO (Belloche et al. 2017), cosmic ray-induced photo-dissociation of NH_2CHO as another possible formation route of HNCHO (Belloche et al. 2017; Ligterink et al. 2018). Consequently, the production of trans-N- CH_3NHCHO largely depend on the availability of HNCHO which may not be formed efficiently or could be easily consumed in the formation of other molecules. As indicated in brown shaded area and yellow dashed line in the upper-middle panel of Figure 7-(b-i), chemical models yield a ratio of trans-N- $\text{CH}_3\text{NHCHO}/\text{NH}_2\text{CHO}$ nearly an order of magnitude lower than the observational values.

In the chemical model of Belloche et al. (2017), trans-N- CH_3NHCHO is proposed to also form via hydrogenation of methyl isocyanate (CH_3NCO):



However, Ligterink et al. (2018) have cast doubt on this pathway based on the non-detection of trans-N- CH_3NHCHO in laboratory ice experiments whilst CH_3NCO was formed abundantly. With the secure detection of trans-N- CH_3NHCHO for the first time in ISM towards Sgr B2 (N1S), chemical models of Belloche et al. (2019) indicated that hydrogenation dominates in trans-N- CH_3NHCHO formation. The best matching model resulted in a trans-N- $\text{CH}_3\text{NHCHO}/\text{CH}_3\text{NCO}$ ratio of 0.23 which is denoted as yellow dashed line in Figure 7-(b-ii). The ratio obtained from observations towards different sources is consistent within the uncertainties of the modelling results, implying that the hydrogenation of CH_3NCO is one plausible source of trans-N- CH_3NHCHO production on grain surfaces. The same chemical network of trans-N- CH_3NHCHO has also been adopted in Garrod et al. (2022), but the trans-N- $\text{CH}_3\text{NHCHO}/\text{CH}_3\text{NCO}$ ratio ranged between 7 to 24. The authors noted that the activation-energy barriers of the grain-surface reaction for CH_3NCO production are poorly defined, which results in substantially under-production of CH_3NCO .

Alternatively, Frigge et al. (2018) demonstrated the formation of trans-N- CH_3NHCHO via reaction (18) in a mixture of methylamine (CH_3NH_2) and CO ices where the HNCH_3 radical is created from CH_3NH_2 by irradiation with energetic electrons i.e. by simulating cosmic rays.



Using the column density of CH_3NH_2 derived towards G+0.693 by Zeng et al. (2018), the $\text{CH}_3\text{C(O)NH}_2/\text{CH}_3\text{NH}_2$ ratio is ~ 0.01 . The comparison of this ratio is currently not available as detections of CH_3NH_2 are very limited in the literature, especially towards the same emitting regions with similar spatial resolution. For instance, CH_3NH_2 has been reported towards Sgr B2(N) using single-dish

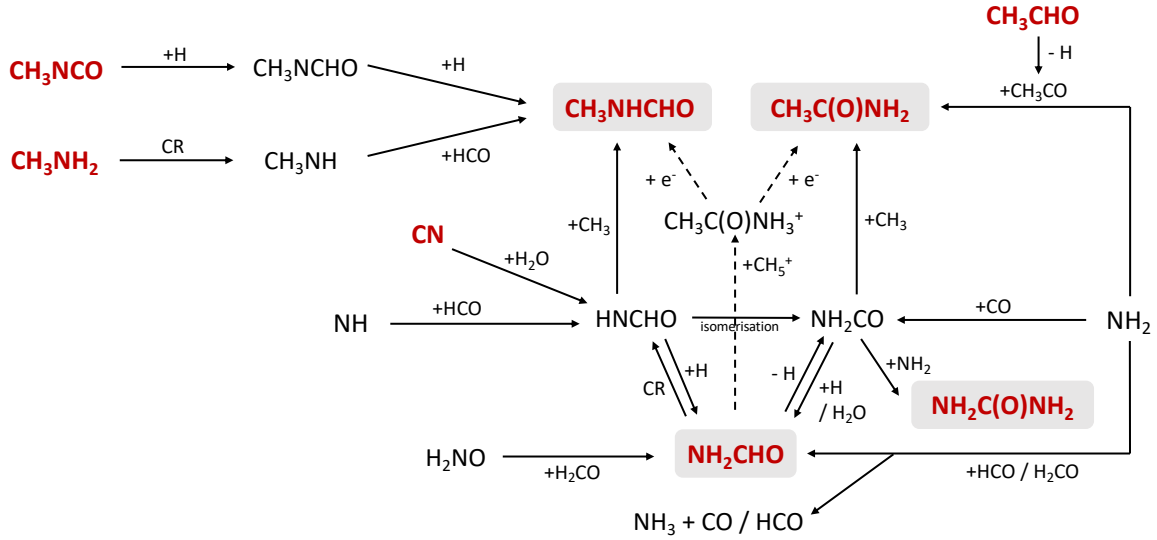


Figure 8. Summary of the proposed chemical formation routes of formamide, acetamide, trans-N-methylformamide, and urea in the ISM. Red denotes the molecular species detected towards G+0.693 molecular cloud and the grey shaded area denotes the amides species studied in this work. The solid and dashed arrows indicate surface chemistry reactions and gas-phase chemistry, respectively.

observations (Belloche et al. 2013) whilst the emission of trans-N-CH₃NHCHO is detected towards Sgr B2(N1S) and Sgr B2(N2) with ALMA (Belloche et al. 2019). Furthermore, high abundance of trans-N-CH₃NHCHO has been reported in G31.41 but the existence of CH₃NH₂ is not yet clear (Ohishi et al. 2019). Increasing the number of trans-N-CH₃NHCHO detections together with NH₂CHO, CH₃NCO, and CH₃NH₂ will better constrain the chemical models and unravel the contributions of different formation pathways.

4.4 Urea

Up to date, G+0.693 is the only other source besides Sgr B2(N1S) where NH₂C(O)NH₂ is securely detected (Belloche et al. 2019; Jiménez-Serra et al. 2020). In this work, the derived NH₂C(O)NH₂/NH₂CHO ratio is 0.030±0.003 which is consistent to the tentative detection towards NGC 6334I MM1-v (~0.03 Ligterink et al. 2020) but a factor of ~3 higher than the one obtained in Sgr B2(N1S) (0.009; Belloche et al. 2019). The comparison is shown in Figure 7-(c).

The chemical model by Belloche et al. (2019) considered NH₂C(O)NH₂ is formed directly by reaction (19) in the grain-surface ices:



It has also been suggested to be one of the most promising formation pathways for NH₂C(O)NH₂ in both experimental and computational studies (Ligterink et al. 2018; Slate et al. 2020). However, as mentioned in Section 4.2, the formation of NH₂CO radical is still a subject of debate. Unlike the case of CH₃C(O)NH₂, there is no information about the relative abundance between NH₂C(O)NH₂ and NH₂CHO in the laboratory experiment by Ligterink et al. (2018). Thus, it is unclear if a consistent result can be found between observation towards G+0.693 and the experimental studies for NH₂C(O)NH₂. On the other hand, the NH₂C(O)NH₂/NH₂CHO ratio derived in G+0.693 is marginally consistent with the value estimated by the fast model of Belloche et al. (2019) (~0.039; see yellow dotted line in Figure

7-(c)). However, the ratio from the medium model of Garrod et al. (2022), which appears to reproduce best other amide species, is at least a factor of a few higher than observed. This indicates that the formation pathways considered may be too efficient on the grains. It was pointed out by the authors that a higher barrier to the production of NH₂ from H-abstraction of ammonia and an efficient destruction route in the gas phase would help to ameliorate the disagreement. Furthermore, the fast model of Belloche et al. (2019) revealed that the solid-phase urea is seen to be produced most strongly after around 55 K, which is the temperature of rapid production and diffusion of NH₂ radical. Owing to the fact that the dust temperature in G+0.693 is low, a higher ratio of NH₂C(O)NH₂/NH₂CHO derived towards G+0.693 in comparison to Sgr B2 (N1S) suggests that either another formation route might be at play at lower temperatures, or a destruction route at high temperature in the gas phase.

Besides radicals, formation pathways involving charged species have been put forward to produce NH₂C(O)NH₂ in the ISM. Theoretical calculation by Jeanvoine & Spezia (2019) proposed that the reaction of protonated hydroxylamine (NH₂OH₂⁺) with neutral NH₂CHO could be one alternative route. Whilst the authors concluded that this pathway would not be readily accessible in the gas phase without certain conditions being met, the presence of ice mantle may facilitate the overall reaction process. The neutral hydroxylamine (NH₂OH) is detected with an abundance of 2.1×10⁻¹⁰ (Rivilla et al. 2020) towards G+0.693, but it is unclear how efficient its cation can be formed on grain surfaces. In addition, the ion-molecule reaction between N-protonated isocyanic acid (H₂NCO⁺) and NH₃ have considered to be responsible for the NH₂C(O)NH₂ formation, both in the gas phase and solid state (Slate et al. 2020, and references therein). With the H₂NCO⁺ abundance of ~10⁻¹¹ derived towards G+0.693 (Rodríguez-Almeida et al. 2021a), which is lower than the one derived for NH₂C(O)NH₂, this route therefore does not appear to be viable in G+0.693.

At present, the formation of NH₂C(O)NH₂ in the ISM is best described by the particular radical-radical reaction of NH₂CO and NH₂. Further exploration of not only ion-molecule reactions on the

grain surfaces but also gas-phase formation route of $\text{NH}_2\text{C}(\text{O})\text{NH}_2$, which has not been given a great deal of attention, are required to improve our understanding of the $\text{NH}_2\text{C}(\text{O})\text{NH}_2$ chemistry in the ISM.

5 CONCLUSIONS

In this work the amide inventory of the Galactic Centre molecular cloud G+0.693 is studied. As a molecular cloud that is proposed to be on the verge of star formation, G+0.693 is a well-suited testbed to study the interstellar chemistry at an early evolutionary stage. With high-sensitivity observations, the robust detection of all NH_2CHO , $\text{CH}_3\text{C}(\text{O})\text{NH}_2$, trans-N- CH_3NHCHO , and $\text{NH}_2\text{C}(\text{O})\text{NH}_2$ is reported, for the first time, towards a region that does not show any star-formation activities. Abundances of amides, derived with respect to H_2 and NH_2CHO , are compared with those obtained across various astronomical sources. The column density ratios of amide species with respect to NH_2CHO do not vary more than an order of magnitude regardless of physical conditions of different sources. This suggests that they are either chemically linked to NH_2CHO or share a common chemical origin with NH_2CHO . Based on the current available literature, the formation pathway of the amide species discussed in the study are generally dominated by grain surface chemistry but the specific chemical process(es) are unclear. However the rather constant abundance ratios found between G+0.693 and star-forming regions suggests that the amide related chemistry, which drives the observed relative abundances, are already set in early evolutionary stages of molecular cloud, and star formation process neither destroys these ratios, nor enhances them through the warm up process. One way to gain insight would be by constraining the formation route of the key precursor, the NH_2CO radical. Considering that several precursors have been detected in G+0.693, attention should not be limited to NH_2CHO but should be to alternative routes involving other molecular species. The prolific amide inventory in G+0.693 confirms it is one of the largest molecular repositories of very complex molecules in the Galaxy.

ACKNOWLEDGEMENTS

We would like to thank Miguel Sanz-Novo and Juan García de la Concepción for helpful discussions. We thank the anonymous referee for a constructive report that improved the quality of this manuscript. We are grateful to the IRAM 30m telescope staff for their help during the different observing runs. IRAM is supported by INSU/CNRS (France), MPG (Germany) and IGN (Spain). We thank Arnaud Belloche and Vadim Ilyushin for providing us the spectroscopic entry of $\text{CH}_3\text{C}(\text{O})\text{NH}_2$ and trans-N- CH_3NHCHO . V.M.R. has received support from the project RYC2020-029387-I funded by MCIN/AEI/10.13039/501100011033, and from the Comunidad de Madrid through the Atracción de Talento Investigador Modalidad I (Doctores con experiencia) Grant (COOL: Cosmic Origins Of Life; 2019-T1/TIC-5379). I.J.-S., J.M.-P. and L. C. acknowledge support from grant No. PID2019-105552RB-C41 by the Spanish Ministry of Science and Innovation/State Agency of Research MCIN/AEI/10.13039/501100011033 and by "ERDF A way of making Europe". P.d.V. and B.T. thank the support from the Spanish Ministerio de Ciencia e Innovación (MICIU) through project PID2019-107115GB-C21. B.T. also acknowledges the Spanish MICIU for funding support from grant PID2019-106235GB-I00.

DATA AVAILABILITY

The data underlying this article will be shared on reasonable request to the corresponding author.

REFERENCES

- Altwegg K., et al., 2016, *Science Advances*, **2**, e1600285
- Barone V., Latouche C., Skouteris D., Vazart F., Balucani N., Ceccarelli C., Lefloch B., 2015, *MNRAS*, **453**, L31
- Belloche A., Müller H. S. P., Menten K. M., Schilke P., Comito C., 2013, *A&A*, **559**, A47
- Belloche A., et al., 2017, *A&A*, **601**, A49
- Belloche A., Garrod R. T., Müller H. S. P., Menten K. M., Medvedev I., Thomas J., Kisiel Z., 2019, *A&A*, **628**, A10
- Bizzocchi L., et al., 2020, *A&A*, **640**, A98
- Blanco S., López J. C., Lesarri A., Alonso J. L., 2006, *Journal of the American Chemical Society*, **128**, 12111
- Bonfand M., Belloche A., Menten K. M., Garrod R. T., Müller H. S. P., 2017, *A&A*, **604**, A60
- Bouscasse L., Csengeri T., Belloche A., Wyrowski F., Bontemps S., Güsten R., Menten K. M., 2022, *A&A*, **662**, A32
- Brown R. D., Godfrey P. D., Storey J., 1975, *Journal of Molecular Spectroscopy*, **58**, 445
- Cernicharo J., et al., 2016, *A&A*, **587**, L4
- Chuang K. J., Jäger C., Krasnokutski S. A., Fulvio D., Henning T., 2022, *ApJ*, **933**, 107
- Colzi L., et al., 2021, *A&A*, **653**, A129
- Colzi L., et al., 2022, *ApJ*, **926**, L22
- Coutens A., et al., 2016, *A&A*, **590**, L6
- Douglas K. M., Lucas D., Walsh C., West N. A., Blitz M. A., Heard D. E., 2022, arXiv e-prints, p. arXiv:2208.12658
- Dulieu F., Nguyen T., Congiu E., Baouche S., Taquet V., 2019, *MNRAS*, **484**, L119
- Endres C. P., Schlemmer S., Schilke P., Stutzki J., Müller H. S. P., 2016, *Journal of Molecular Spectroscopy*, **327**, 95
- Fedoseev G., Chuang K. J., van Dishoeck E. F., Ioppolo S., Linnartz H., 2016, *MNRAS*, **460**, 4297
- Frigge R., et al., 2018, *ApJ*, **862**, 84
- GRAVITY Collaboration et al., 2019, *A&A*, **625**, L10
- Gardner F. F., Godfrey P. D., Williams D. R., 1980, *MNRAS*, **193**, 713
- Garrod R. T., Jin M., Matis K. A., Jones D., Willis E. R., Herbst E., 2022, *ApJS*, **259**, 1
- Gorai P., Bhat B., Sil M., Mondal S. K., Ghosh R., Chakrabarti S. K., Das A., 2020, *ApJ*, **895**, 86
- Guzmán A. E., Sanhueza P., Contreras Y., Smith H. A., Jackson J. M., Hoq S., Rathborne J. M., 2015, *ApJ*, **815**, 130
- Halfen D. T., Ilyushin V., Ziurys L. M., 2011, *ApJ*, **743**, 60
- Hasegawa T., Sato F., Whiteoak J. B., Miyawaki R., 1994, *ApJ*, **429**, L77
- Haupa K. A., Tarczay G., Lee Y.-P., 2019, *Journal of the American Chemical Society*, **141**, 11614
- Hirota E., Sugisaki R., Nielsen C. J., Sørensen G. O., 1974, *Journal of Molecular Spectroscopy*, **49**, 251
- Hollis J. M., Lovas F. J., Remijan A. J., Jewell P. R., Ilyushin V. V., Kleiner I., 2006, *ApJ*, **643**, L25
- Ilyushin V. V., Alekseev E. A., Dyubko S. F., Kleiner I., Hougen J. T., 2004, *Journal of Molecular Spectroscopy*, **227**, 115
- Jeanvoine Y., Spezia R., 2019, *Theor Chem Acc*, **138**, 1
- Jiménez-Serra I., et al., 2020, *Astrobiology*, **20**, 1048
- Jiménez-Serra I., et al., 2022, *A&A*, **663**, A181
- Jones B. M., Bennett C. J., Kaiser R. I., 2011, *ApJ*, **734**, 78
- Kasten W., Dreizler H., 1986, *Zeitschrift Naturforschung Teil A*, **41**, 1173
- Kawashima Y., Usami T., Suenram R. D., Golubiatnikov G. Y., Hirota E., 2010, *Journal of Molecular Spectroscopy*, **263**, 11
- Kretschmer U., Consalvo D., Knaack A., Schade W., Stahl W., Dreizler H., 1996, *Molecular Physics*, **87**, 1159

- Kryvda A. V., Gerasimov V. G., Dyubko S. F., Alekseev E. A., Motiyenko R. A., 2009, *Journal of Molecular Spectroscopy*, **254**, 28
- Kukulich S. G., Nelson A. C., 1971, *Chemical Physics Letters*, **11**, 383
- Ligterink N. F. W., Terwisscha van Scheltinga J., Taquet V., Jørgensen J. K., Cazaux S., van Dishoeck E. F., Linnartz H., 2018, *MNRAS*, **480**, 3628
- Ligterink N. F. W., El-Abd S. J., Brogan C. L., Hunter T. R., Remijan A. J., Garrod R. T., McGuire B. M., 2020, *ApJ*, **901**, 37
- Ligterink N. F. W., et al., 2022, *ACS Earth and Space Chemistry*, **6**, 455
- López-Sepulcre A., et al., 2015, *MNRAS*, **449**, 2438
- López-Sepulcre A., Balucani N., Ceccarelli C., Codella C., Dulieu F., Theulé P., 2019, *ACS Earth and Space Chemistry*, **3**, 2122
- Lykke J. M., et al., 2017, *A&A*, **597**, A53
- Martín-Doménech R., Rivilla V. M., Jiménez-Serra I., Quénard D., Testi L., Martín-Pintado J., 2017, *MNRAS*, **469**, 2230
- Martín S., Requena-Torres M. A., Martín-Pintado J., Mauersberger R., 2008, *ApJ*, **678**, 245
- Martín S., Martín-Pintado J., Blanco-Sánchez C., Rivilla V. M., Rodríguez-Franco A., Rico-Villas F., 2019, *A&A*, **631**, A159
- Mendoza E., Lefloch B., López-Sepulcre A., Ceccarelli C., Codella C., Boechat-Roberty H. M., Bachiller R., 2014, *MNRAS*, **445**, 151
- Moskienko E. M., Dyubko S. F., 1991, *Radiophysics and Quantum Electronics*, **34**, 181
- Motiyenko R. A., Tercero B., Cernicharo J., Margulès L., 2012, *A&A*, **548**, A71
- Noble J. A., et al., 2015, *A&A*, **576**, A91
- Ohishi M., Suzuki T., Hirota T., Saito M., Kaifu N., 2019, *PASJ*, **71**, 86
- Patel B. H., Percivalle C., Ritson D. J., Duffy C. D., Sutherland J. D., 2015, *Nature Chemistry*, **7**, 301
- Pickett H. M., Poynter R. L., Cohen E. A., Delitsky M. L., Pearson J. C., Müller H. S. P., 1998, *J. Quant. Spectrosc. Radiative Transfer*, **60**, 883
- Quénard D., Jiménez-Serra I., Viti S., Holdship J., Coutens A., 2018, *MNRAS*, **474**, 2796
- Redondo P., Barrientos C., Largo A., 2014, *ApJ*, **793**, 32
- Remijan A. J., et al., 2014, *ApJ*, **783**, 77
- Remijan A., et al., 2022, *A&A*, **658**, A85
- Requena-Torres M. A., Martín-Pintado J., Rodríguez-Franco A., Martín S., Rodríguez-Fernández N. J., de Vicente P., 2006, *A&A*, **455**, 971
- Requena-Torres M. A., Martín-Pintado J., Martín S., Morris M. R., 2008, *ApJ*, **672**, 352
- Rimola A., Skouteris D., Balucani N., Ceccarelli C., Enrique-Romero J., Taquet V., Ugliengo P., 2018, *ACS Earth and Space Chemistry*, **2**, 720
- Rivilla V. M., et al., 2018, *MNRAS*, **475**, L30
- Rivilla V. M., et al., 2019, *MNRAS*, **483**, L114
- Rivilla V. M., et al., 2020, *ApJ*, **899**, L28
- Rivilla V. M., et al., 2021a, *Proceedings of the National Academy of Science*, **118**, e2101314118
- Rivilla V. M., et al., 2021b, *MNRAS*, **506**, L79
- Rivilla V. M., et al., 2022a, *Frontiers in Astronomy and Space Sciences*, **9**, 829288
- Rivilla V. M., et al., 2022b, *Frontiers in Astronomy and Space Sciences*, **9**, 876870
- Rivilla V. M., et al., 2022c, *ApJ*, **929**, L11
- Rodríguez-Almeida L. F., et al., 2021a, *A&A*, **654**, L1
- Rodríguez-Almeida L. F., et al., 2021b, *ApJ*, **912**, L11
- Rodríguez-Fernández N. J., Martín-Pintado J., Fuente A., Wilson T. L., 2004, *A&A*, **427**, 217
- Rubin R. H., Swenson G. W. J., Benson R. C., Tigelaar H. L., Flygare W. H., 1971, *ApJ*, **169**, L39
- Ruiz-Mirazo K., Briones C., de la Escosura A., 2014, *Chemical Reviews*, **114**, 285
- Sanz-Novo M., et al., 2022, arXiv e-prints, p. arXiv:2203.07334
- Skouteris D., Vazart F., Ceccarelli C., Balucani N., Puzzarini C., Barone V., 2017, *MNRAS*, **468**, L1
- Slate E. C. S., Barker R., Euesden R. T., Revels M. R., Meijer A. J. H. M., 2020, *MNRAS*, **497**, 5413
- Song L., Kästner J., 2016, *Physical Chemistry Chemical Physics (Incorporating Faraday Transactions)*, **18**, 29278
- Stubgaard M., 1978, PhD thesis, Københavns Universitet
- Taquet V., López-Sepulcre A., Ceccarelli C., Neri R., Kahane C., Charnley S. B., 2015, *ApJ*, **804**, 81
- Tsuboi M., Miyazaki A., Uehara K., 2015, *PASJ*, **67**, 90
- Vorob'eva E. M., Dyubko S. F., 1994, *Radiophysics and Quantum Electronics*, **37**, 155
- Zeng S., et al., 2018, *MNRAS*, **478**, 2962
- Zeng S., et al., 2020, *MNRAS*, **497**, 4896
- Zeng S., et al., 2021, *ApJ*, **920**, L27

APPENDIX A: MOLECULAR SPECTROSCOPY

Table A1. Line list and spectroscopic references for the molecules studied in this work

Molecule	Catalogue	Entry	Date	Reference
NH ₂ CHO	CDMS	45512	April 2013	(1), (2), (3), (4), (5), (6), (7), (8)
NH ₂ ¹³ CHO	CDMS	46512	April 2013	(3), (6), (7), (8), (9)
CH ₃ C(O)NH ₂	This work	–	December 2020	(10), (11)
trans-N-CH ₃ NHCHO	This work	–	December 2020	(11)
NH ₂ C(O)NH ₂	CDMS	60517	October 2017	(12), (13), (14), (15)

Notes. The species labelled with MADCUBA were imported into MADCUBA, using the spectroscopic works indicated in the table.

References. (1)Kukolich & Nelson (1971); (2)Hirota et al. (1974); (3)Gardner et al. (1980); (4)Moskienko & Dyubko (1991); (5)Vorob'eva & Dyubko (1994); (6)Blanco et al. (2006); (7)Kryvda et al. (2009); (8)Motiyenko et al. (2012); (9)Stubgaard (1978); (10)Ilyushin et al. (2004); (11)Belloche et al. (2017); (12)Remijan et al. (2014); (13)Brown et al. (1975); (14)Kasten & Dreizler (1986); (15)Kretschmer et al. (1996)

Table A2: List of detected unblended or slightly blended transitions of the amides analysed in this work. The columns indicate the frequency, quantum numbers, logarithm of the integrated intensity at 300 K, energy of the upper levels of each transition (E_u), and information about the possible blending by other identified or unidentified (U) species towards G+0.693. Asterisk (*) indicates the transitions detected in previous studies towards G+0.693.

Molecule	Frequency (GHz)	Transition		logI(300K) (nm ² MHz)	E_u (K)	Blending
		($J''_{K''_a, K''_c} - J'_{K'_a, K'_c}$)	E/A)			
CH ₃ C(O)NH ₂	32.640032	3 _{0,3} -2 _{1,2}	E	-6.344	9.71	unblended or blended with U
CH ₃ C(O)NH ₂	35.226603	4 _{3,2} -3 _{3,1}	E	-6.687	15.04	unblended
CH ₃ C(O)NH ₂	39.338502	3 _{1,3} -2 _{0,2}	E	-6.137	9.74	unblended or blended with U
CH ₃ C(O)NH ₂	40.755758	5 _{1,4} -5 _{0,5}	E	-6.285	16.67	unblended
CH ₃ C(O)NH ₂	46.534292	4 _{0,4} -3 _{1,3}	E	-5.668	11.98	unblended
CH ₃ C(O)NH ₂	77.317157	3 _{0,3} -2 _{1,2}	E	-6.476	13.45	unblended
CH ₃ C(O)NH ₂	77.329953	7 _{0,7} -6 _{1,6}	E	-4.950	21.64	unblended
CH ₃ C(O)NH ₂	77.330094	7 _{1,7} -6 _{1,6}	E	-6.473	21.64	unblended
CH ₃ C(O)NH ₂	77.331133	7 _{0,7} -6 _{0,6}	E	-6.473	21.64	unblended
CH ₃ C(O)NH ₂	77.331275	7 _{1,7} -6 _{0,6}	E	-4.950	21.64	unblended
CH ₃ C(O)NH ₂	77.900349	3 _{3,0} -2 _{2,0}	E	-5.404	14.90	unblended
CH ₃ C(O)NH ₂	87.604693	8 _{0,8} -7 _{1,7}	E	-4.785	25.85	shoulder of HNCO and HN ¹³ CO
CH ₃ C(O)NH ₂	87.604710	8 _{1,8} -7 _{1,7}	E	-6.252	25.85	shoulder of HNCO and HN ¹³ CO
CH ₃ C(O)NH ₂	87.604835	8 _{0,8} -7 _{0,7}	E	-6.252	25.85	shoulder of HNCO and HN ¹³ CO
CH ₃ C(O)NH ₂	87.604852	8 _{1,8} -7 _{0,7}	E	-4.785	25.85	shoulder of HNCO and HN ¹³ CO
CH ₃ C(O)NH ₂	93.680900	6 _{3,4} -5 _{2,3}	E	-5.187	22.36	unblended
CH ₃ C(O)NH ₂	97.810915	8 _{1,7} -7 _{2,6}	E	-4.771	29.32	blended with Ga-n-C ₃ H ₇ OH
CH ₃ C(O)NH ₂	97.812712	8 _{2,7} -7 _{2,6}	E	-6.242	29.32	blended with Ga-n-C ₃ H ₇ OH
CH ₃ C(O)NH ₂	97.823791	8 _{1,7} -7 _{1,6}	E	-6.243	29.32	blended with H ₂ CCCHCN
CH ₃ C(O)NH ₂	97.825588	8 _{2,7} -7 _{1,6}	E	-4.771	29.32	blended with H ₂ CCCHCN
CH ₃ C(O)NH ₂	97.893420	9 _{0,9} -8 _{1,8}	E	-4.640	30.54	blended with aGg'-(CH ₂ OH) ₂
CH ₃ C(O)NH ₂	97.893422	9 _{1,9} -8 _{1,8}	E	-6.069	30.54	blended with aGg'-(CH ₂ OH) ₂
CH ₃ C(O)NH ₂	97.893437	9 _{0,9} -8 _{0,8}	E	-6.069	30.54	blended with aGg'-(CH ₂ OH) ₂
CH ₃ C(O)NH ₂	97.893439	9 _{1,9} -8 _{0,8}	E	-4.640	30.54	blended with aGg'-(CH ₂ OH) ₂
CH ₃ C(O)NH ₂	98.113341	4 _{4,0} -3 _{3,0}	E	-5.055	19.61	unblended
CH ₃ C(O)NH ₂	107.988285	9 _{1,8} -8 _{2,7}	E	-4.626	34.51	unblended
CH ₃ C(O)NH ₂	107.990327	9 _{2,8} -8 _{1,7}	E	-4.626	34.51	unblended
CH ₃ C(O)NH ₂	108.190197	10 _{0,10} -9 _{1,9}	E	-4.511	35.74	unblended
CH ₃ C(O)NH ₂	108.190197	10 _{1,10} -9 _{1,9}	E	-5.912	35.74	unblended
CH ₃ C(O)NH ₂	108.190199	10 _{0,10} -9 _{0,9}	E	-5.912	35.74	unblended
CH ₃ C(O)NH ₂	108.190200	10 _{1,10} -9 _{0,9}	E	-4.511	35.74	unblended
CH ₃ C(O)NH ₂	108.606162	8 _{3,6} -7 _{2,5}	E	-4.784	32.27	unblended
CH ₃ C(O)NH ₂	109.349123	5 _{4,1} -4 _{3,1}	E	-5.266	21.54	blended with aGg'-(CH ₂ OH) ₂
CH ₃ C(O)NH ₂	113.867594	5 _{5,1} -4 _{4,1}	E	-4.993	23.30	share with CH ₃ C(O)NH ₂ 7 _{4,4} -6 _{3,3} A
CH ₃ C(O)NH ₂	34.987857	6 _{5,2} -6 _{4,3}	A	-5.997	20.20	blended with anti-C ₂ H ₅ NH ₂
CH ₃ C(O)NH ₂	34.989515	4 _{1,3} -4 _{0,4}	A	-6.372	7.61	blended with anti-C ₂ H ₅ NH ₂
CH ₃ C(O)NH ₂	40.302903	3 _{1,2} -2 _{2,1}	A	-6.417	4.84	unblended or blended with U
CH ₃ C(O)NH ₂	46.312309	4 _{0,4} -3 _{1,3}	A	-5.662	5.93	unblended
CH ₃ C(O)NH ₂	46.449611	2 _{2,0} -1 _{1,1}	A	-6.262	3.03	blended with H ₂ CCCHCN
CH ₃ C(O)NH ₂	46.450396	4 _{0,4} -3 _{0,3}	A	-6.844	5.93	blended with H ₂ CCCHCN
CH ₃ C(O)NH ₂	46.473480	4 _{1,4} -3 _{0,3}	A	-5.658	5.93	unblended
CH ₃ C(O)NH ₂	74.172527	4 _{3,2} -3 _{2,1}	A	-5.479	9.00	unblended or blended with U
CH ₃ C(O)NH ₂	77.199071	6 _{1,5} -5 _{2,4}	A	-5.136	14.56	blended with U
CH ₃ C(O)NH ₂	77.320853	7 _{0,7} -6 _{1,6}	A	-4.951	15.58	unblended
CH ₃ C(O)NH ₂	77.320920	7 _{1,7} -6 _{1,6}	A	-6.153	15.58	unblended
CH ₃ C(O)NH ₂	77.321347	7 _{0,7} -6 _{0,6}	A	-6.153	15.58	unblended
CH ₃ C(O)NH ₂	77.321414	7 _{1,7} -6 _{0,6}	A	-4.950	15.58	unblended
CH ₃ C(O)NH ₂	77.435420	6 _{2,5} -5 _{1,4}	A	-5.133	14.56	unblended or blended with U
CH ₃ C(O)NH ₂	82.338160	5 _{3,3} -4 _{2,2}	A	-5.341	12.59	unblended
CH ₃ C(O)NH ₂	85.746007	6 _{2,4} -5 _{3,3}	A	-5.221	16.70	blended with C ₂ H ₅ OH
CH ₃ C(O)NH ₂	87.586466	7 _{1,6} -6 _{2,5}	A	-4.938	18.76	blended with H ₂ CCCHCN
CH ₃ C(O)NH ₂	87.623526	7 _{1,6} -6 _{1,5}	A	-6.098	18.76	unblended
CH ₃ C(O)NH ₂	87.629757	7 _{2,6} -6 _{1,5}	A	-4.937	18.76	unblended

Continued on next page

Table A2 – *Continued from previous page*

Molecule	Frequency (GHz)	Transition ($J''_{K''_a, K''_c} - J'_{K'_a, K'_c}$ E/A)	$\log I(300\text{K})$ (nm^2MHz)	E_u (K)	Blending
CH ₃ C(O)NH ₂	87.632434	8 _{0,8} -7 _{1,7} A	-4.784	19.79	unblended
CH ₃ C(O)NH ₂	87.632443	8 _{1,8} -7 _{1,7} A	-5.989	19.79	unblended
CH ₃ C(O)NH ₂	87.632501	8 _{0,8} -7 _{0,7} A	-5.989	19.79	unblended
CH ₃ C(O)NH ₂	87.632510	8 _{1,8} -7 _{0,7} A	-4.784	19.79	unblended
CH ₃ C(O)NH ₂	97.905697	8 _{1,7} -7 _{2,6} A	-4.77	23.46	unblended
CH ₃ C(O)NH ₂	97.906677	8 _{2,7} -7 _{2,6} A	-5.941	23.46	unblended
CH ₃ C(O)NH ₂	97.911929	8 _{1,7} -7 _{1,6} A	-5.941	23.46	unblended
CH ₃ C(O)NH ₂	97.912908	8 _{2,7} -7 _{1,6} A	-4.77	23.46	unblended
CH ₃ C(O)NH ₂	97.943873	9 _{0,9} -8 _{1,8} A	-4.639	24.49	unblended
CH ₃ C(O)NH ₂	97.943874	9 _{1,9} -8 _{1,8} A	-5.846	24.49	unblended
CH ₃ C(O)NH ₂	97.943882	9 _{0,9} -8 _{0,8} A	-5.846	24.49	unblended
CH ₃ C(O)NH ₂	97.943883	9 _{1,9} -8 _{0,8} A	-4.639	24.49	unblended
CH ₃ C(O)NH ₂	108.214105	9 _{1,8} -8 _{2,7} A	-4.625	28.66	blended with C ₂ H ₅ CN
CH ₃ C(O)NH ₂	108.214251	9 _{2,8} -8 _{2,7} A	-5.803	28.66	blended with C ₂ H ₅ CN
CH ₃ C(O)NH ₂	108.215083	9 _{1,8} -8 _{1,7} A	-5.803	28.66	blended with C ₂ H ₅ CN
CH ₃ C(O)NH ₂	108.215230	9 _{2,8} -8 _{1,7} A	-4.625	28.66	blended with C ₂ H ₅ CN
CH ₃ C(O)NH ₂	108.255232	10 _{0,10} -9 _{1,9} A	-4.51	29.68	unblended
CH ₃ C(O)NH ₂	108.255232	10 _{1,10} -9 _{1,9} A	-5.719	29.68	unblended
CH ₃ C(O)NH ₂	108.255234	10 _{0,10} -9 _{0,9} A	-5.719	29.68	unblended
CH ₃ C(O)NH ₂	108.255234	10 _{1,10} -9 _{0,9} A	-4.510	29.68	unblended
CH ₃ C(O)NH ₂	110.952601	5 _{5,1} -4 _{4,0} A	-4.828	15.69	blended with CH ₃ COOH
CH ₃ C(O)NH ₂	113.868958	7 _{4,4} -6 _{3,3} A	-4.972	23.61	share with CH ₃ C(O)NH ₂ 5 _{5,1} -4 _{4,1} E
CH ₃ C(O)NH ₂	139.138720	12 _{1,11} -11 _{2,10} A	-4.281	47.21	blended with HCCCH ₂ CN
CH ₃ C(O)NH ₂	139.138723	12 _{2,11} -11 _{1,10} A	-4.281	47.21	blended with HCCCH ₂ CN
CH ₃ C(O)NH ₂	139.188418	13 _{0,13} -12 _{1,12} A	-4.199	48.24	unblended
CH ₃ C(O)NH ₂	139.188418	13 _{1,13} -12 _{0,12} A	-4.199	48.24	unblended
trans-N-CH ₃ NHCHO	32.550890	3 _{1,3} -2 _{1,2} E	-6.223	7.48	unblended
trans-N-CH ₃ NHCHO	33.455906	3 _{0,3} -2 _{0,2} A	-6.154	3.23	unblended
trans-N-CH ₃ NHCHO	34.461458	3 _{1,2} -2 _{1,1} E	-6.230	8.42	unblended
trans-N-CH ₃ NHCHO	34.693486	2 _{1,2} -1 _{0,1} A	-6.537	2.21	unblended
trans-N-CH ₃ NHCHO	37.428359	4 _{2,2} -4 _{1,3} A	-6.200	8.26	blended with C ₆ H
trans-N-CH ₃ NHCHO	39.138171	3 _{2,1} -3 _{1,2} A	-6.343	6.04	blended with U
trans-N-CH ₃ NHCHO	43.793726	3 _{1,3} -2 _{0,2} A	-6.199	3.72	unblended
trans-N-CH ₃ NHCHO	44.092441	4 _{0,4} -3 _{0,3} A	-5.793	5.34	unblended
trans-N-CH ₃ NHCHO	45.131824	4 _{2,3} -3 _{2,2} A	-5.899	8.18	unblended
trans-N-CH ₃ NHCHO	46.120191	5 _{0,5} -4 _{1,4} A	-3.990	7.95	blended with HOCH ₂ CN
trans-N-CH ₃ NHCHO	72.670325	7 _{1,7} -6 _{1,6} A	-5.135	14.74	unblended
trans-N-CH ₃ NHCHO	74.090940	7 _{0,7} -6 _{0,6} A	-5.115	14.60	unblended
trans-N-CH ₃ NHCHO	74.122946	7 _{0,7} -6 _{0,6} E	-5.094	18.24	blended with ¹³ CH ₂ CHCN
trans-N-CH ₃ NHCHO	79.741415	3 _{2,1} -2 _{1,2} A	-5.847	6.03	unblended
trans-N-CH ₃ NHCHO	82.715063	8 _{1,8} -7 _{1,7} A	-4.969	18.71	blended with H ₂ CCCHCN
trans-N-CH ₃ NHCHO	83.253887	7 _{2,5} -6 _{2,4} A	-5.047	18.45	unblended
trans-N-CH ₃ NHCHO	87.496110	8 _{1,8} -7 _{0,7} E	-5.204	22.44	unblended
trans-N-CH ₃ NHCHO	89.031261	8 _{2,7} -7 _{2,6} A	-4.930	22.13	unblended
trans-N-CH ₃ NHCHO	89.935665	8 _{1,7} -7 _{1,6} E	-4.886	24.61	unblended
trans-N-CH ₃ NHCHO	92.415560	9 _{1,9} -8 _{1,8} E	-4.817	26.87	unblended
trans-N-CH ₃ NHCHO	93.395965	8 _{1,7} -7 _{1,6} A	-4.869	21.18	unblended
trans-N-CH ₃ NHCHO	93.406380	9 _{0,9} -8 _{0,8} A	-4.816	23.10	unblended
trans-N-CH ₃ NHCHO	95.642981	8 _{2,6} -7 _{2,5} A	-4.866	23.04	blended with C ₂ H ₅ OCH ₃
trans-N-CH ₃ NHCHO	105.608314	3 _{3,0} -2 _{2,1} A	-5.362	9.45	unblended
trans-N-CH ₃ NHCHO	107.852547	9 _{2,7} -8 _{2,6} A	-4.712	28.22	unblended
trans-N-CH ₃ NHCHO	109.325438	3 _{3,0} -2 _{2,0} E	-5.314	14.35	unblended
NH ₂ ¹³ CHO	40.778439	2 _{1,2} -1 _{1,1}	-4.664	5.8	unblended
NH ₂ ¹³ CHO	42.318061	2 _{0,2} -1 _{0,1}	-4.503	3.0	unblended
NH ₂ ¹³ CHO	81.495632	4 _{1,4} -3 _{1,3}	-3.674	12.7	unblended
NH ₂ ¹³ CHO	84.390679	4 _{0,4} -3 _{0,3}	-3.612	10.1	unblended
NH ₂ ¹³ CHO	101.813583	5 _{1,5} -4 _{1,4}	-3.379	17.6	unblended

Continued on next page

Table A2 – Continued from previous page

Molecule	Frequency (GHz)	Transition ($J''_{K''_a, K''_c} - J'_{K'_a, K'_c}$ E/A)	$\log I(300K)$ (nm^2MHz)	E_u (K)	Blending
$\text{NH}_2^{13}\text{CHO}$	105.260270	$5_{0,5} - 4_{0,4}$	-3.330	15.2	unblended
$\text{NH}_2\text{C}(\text{O})\text{NH}_2$	37.926700	$3_{0,3} - 2_{0,2}$	-5.011	3.89	unblended
$\text{NH}_2\text{C}(\text{O})\text{NH}_2$	39.116400	$2_{2,1} - 1_{1,0}$	-5.195	2.91	blended with U
$\text{NH}_2\text{C}(\text{O})\text{NH}_2$	48.697422	$4_{0,4} - 3_{1,3}$	-4.648	6.23	unblended
$\text{NH}_2\text{C}(\text{O})\text{NH}_2$	48.705728	$4_{1,4} - 3_{0,3}$	-4.648	6.23	blended with U
* $\text{NH}_2\text{C}(\text{O})\text{NH}_2$	81.104130	$6_{1,5} - 5_{2,4}$	-4.107	15.29	blended with DNCO
* $\text{NH}_2\text{C}(\text{O})\text{NH}_2$	81.108770	$6_{2,5} - 5_{1,4}$	-4.107	15.29	blended with DNCO
* $\text{NH}_2\text{C}(\text{O})\text{NH}_2$	81.199200	$7_{0,7} - 6_{1,6}$	-3.945	16.36	unblended
* $\text{NH}_2\text{C}(\text{O})\text{NH}_2$	81.199200	$7_{1,7} - 6_{0,6}$	-3.945	16.36	unblended
$\text{NH}_2\text{C}(\text{O})\text{NH}_2$	92.031820	$8_{0,8} - 7_{1,7}$	-3.780	20.78	blended with $\text{CH}_2\text{CH}^{13}\text{CN}$
$\text{NH}_2\text{C}(\text{O})\text{NH}_2$	92.031820	$8_{1,8} - 7_{0,7}$	-3.780	20.78	blended with $\text{CH}_2\text{CH}^{13}\text{CN}$
$\text{NH}_2\text{C}(\text{O})\text{NH}_2$	96.185230	$5_{4,2} - 4_{3,1}$	-4.253	14.53	blended with U
* $\text{NH}_2\text{C}(\text{O})\text{NH}_2$	102.76756	$8_{1,7} - 7_{2,6}$	-3.754	24.64	blended with CH_3COCH_3
* $\text{NH}_2\text{C}(\text{O})\text{NH}_2$	102.76756	$8_{2,7} - 7_{1,6}$	-3.754	24.64	blended with CH_3COCH_3
* $\text{NH}_2\text{C}(\text{O})\text{NH}_2$	102.86432	$9_{0,9} - 8_{1,8}$	-3.635	25.71	unblended
* $\text{NH}_2\text{C}(\text{O})\text{NH}_2$	102.86432	$9_{1,9} - 8_{0,8}$	-3.635	25.71	unblended

This paper has been typeset from a $\text{\TeX}/\text{\LaTeX}$ file prepared by the author.